PHYSICAL REVIEW E, VOLUME 65, 066407

Analytic solution for low-frequency rf sheaths in pulsed discharges

F. L. Waelbroeck*
Institute for Fusion Studies, University of Texas, Austin, Texas 78712

(Received 1 February 2002; published 19 June 2002)

The equations governing the evolution of rf-driven sheaths are solved analytically in the regime where the rf frequency is small compared to both the ionic plasma frequency and the ion transit time in the sheaths. Poincaré's map of first return is used to gain geometric insight into the dynamics of the circuit-sheath system. The requirements of minimizing wall bombardment while maximizing the efficiency of the coupling to the substrate sheath are shown to lead to an optimum value for the blocking capacitance in asymmetric discharges. This optimum value is also favorable for rapid relaxation to the steady state in pulsed discharges. The analytic solution is applied to the problem of negative-ion extraction in afterglow plasmas.

DOI: 10.1103/PhysRevE.65.066407 PACS number(s): 52.77.Bn, 52.80.Pi, 52.40.Kh, 52.27.Cm

I. INTRODUCTION

Radio-frequency-driven plasma sheaths are widely used to produce anisotropic fluxes of energetic ions for a variety of applications [1]. In recent years, efforts to improve the efficacy of the related plasma processes have shown that several advantages accrue from pulsing the heating power used to sustain the discharge. In particular, pulsed (square-wave modulated) power has been shown to reduce dust production during etching [2], to allow control (through variation of the duty cycle) of the radical composition and thus of etch selectivity [3], and to enable increased plasma densities at constant heating power [4,5]. Pulsed or modulated power has also been used as a diagnostic method to infer reaction kinetics from observations of density decay rates [2,6,7], and to allow measurements of the electric charge of particulates [8]. Most importantly perhaps, pulsed-power discharges have been shown to produce, during the afterglow phases, plasmas with extremely high electronegativities approximating pure ion-ion plasmas. In such plasmas rf biasing leads to the extraction of equal negative and positive ion charges. This avoids the differential charging of the surface of the substrate with respect to the bottom of the trenches and consequently improves etch anisotropy [9–13].

The use of pulsed power raises more questions, however, concerning the relaxation of the rf-driven sheath oscillations. External circuit elements are known to play an important role in determining sheath dynamics [14,15], but the mechanics of this role is complicated by the nonlinear nature of the sheaths. Numerical simulations have proven useful for investigating sheath dynamics, but the disparity in time and spatial scales between core transport phenomena and the rf frequency requires the use of separate codes for the sheaths and the plasma core [11,16]. Even with this separation, simulations remain onerous. The aim of the present paper is to construct an analytic solution of the equations for the sheath-substrate bias circuit. In addition to providing a highly flexible method for solving sheath dynamics problems in pulsed discharges, the analytic solution yields insight into the mechanisms governing sheath motion, the role of the external circuit elements, and the relaxation behavior of sheaths in pulsed plasma.

Previous investigations of sheath dynamics [17–24] have identified two separate regimes distinguished by the relative magnitudes of the frequency of the applied rf signal and the ion plasma frequency (or equivalently [17], the inverse of the transit time for ions crossing the sheath). In the high-frequency regime [18], the ion properties remain constant in time throughout the sheath, and the current is dominated by the displacement current associated with the tidal motion of the electrons in the ion ''beach.'' The high-frequency regime is thus unsuited to negative-ion energization. In the low-frequency regime [19–21,25–27], by contrast, the instantaneous electron and ion profiles are the same as those in a dc sheath and they evolve adiabatically with the changing bias voltage. For sufficiently high electronegativities it is thus possible to alternate the sign of the sheath bias and successively accelerate negative and positive ions towards the substrate.

In this paper we restrict our consideration to the low-frequency regime. We begin in Sec. II by describing the double-probe model for electron-ion sheaths and deriving a reduced version of this model valid for low frequencies. The reduced model describes the discharge in terms of a single first-order ordinary differential equation. Our analysis extends previous treatments for large [19,20,25–27] and small [17] values of the blocking capacitance, and provides a method for studying relaxation in pulsed discharges. We note that negative ions are confined to the plasma core by ambipolar and sheath potentials even for moderately high electronegativities. The electron-ion double-probe model thus applies whenever the electronegativity is insufficient to cause sheath inversion. In Sec. III we solve our model equation analytically under the assumption that the applied potential is much greater than the electron temperature. This assumption is well satisfied in practice. This leads us to introduce the phase-return map, describing the times at which the ground and chuck (powered electrode) sheaths terminate their successive saturation periods. We use this map in Sec. IV to investigate the steady-state properties as well as the rate of relaxation to steady state in pulsed discharges. In Sec. V we extend the double-probe model to highly electronegative and ion-ion plasmas by using results from the theory of elec-

---

*Email address: flw@mail.utexas.edu

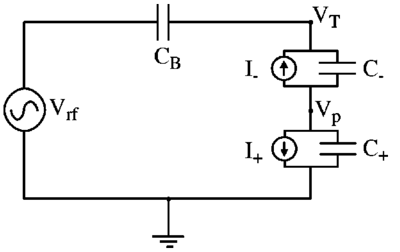

FIG. 1. Equivalent circuit diagram for the MEO model [21].

tronegative sheaths [28–31]. We derive conditions for sheath inversion and discuss the sheath dynamics and the role of the blocking capacitance. We conclude in Sec. VI by summarizing and discussing our results.

II. REDUCED DOUBLE-PROBE MODEL

Double-probe models were introduced by Pointu [19,20] and Metze, Ernie, and Oskam (MEO) [21] to replace phenomenological models of capacitively driven rf sheaths by models based on the known physical properties of plasma sheaths. The central assumption of the double-probe models is that the drive frequency is sufficiently small, so that the instantaneous properties of the sheath are approximately the same as in a stationary or dc sheath. The MEO model is more general than that of Pointu, in that it considers a finite blocking capacitance C_B and allows a consideration of aperiodic or transient conditions.

The equations of the MEO model follow from a straightforward application of Kirchoff's law to the circuit described in Fig. 1. They are

$$\omega C_- \frac{d}{dt}(V_p - V_T) + \omega C_B \frac{d}{dt}(V_{\rm rf} - V_T) + I_- = 0, \quad (1a)$$

$$\omega C_+ \frac{d}{dt} V_p + \omega C_- \frac{d}{dt}(V_p - V_T) + I_+ + I_- = 0. \quad (1b)$$

Here V_p is the plasma potential and V_T is the potential on the target (powered) electrode. The time t has been normalized to the inverse of the angular frequency ω. The subscripts $+$ and $-$ denote quantities describing the grounded and the target sheath, respectively. This notation is motivated by fact that in asymmetric discharges the target electrode plays the role of the cathode during most of the rf period. The I_σ, where $\sigma = \pm$, represent the conduction currents in the sheath. They are given by

$$I_\sigma = I_{i\sigma}(1 - \mathrm{e}^{\varphi_\sigma - \varphi_f}), \quad (2)$$

where $\varphi_\sigma = eV_\sigma / kT_e$ are the normalized electrode potentials with respect to the plasma, $\varphi_f = 1/2 \ln(2\pi m_e/m_i)$ is the floating potential, $I_{i\sigma} = A_\sigma e n_\sigma u_B$ are the ion saturation currents, $u_B = \sqrt{kT_e/m_i}$ is the Bohm velocity, and n_σ are the densities at the entrance of the sheaths. Finally, the $C_\sigma(V_\sigma)$ describe the sheath capacitances. We note that Sobolewski has demonstrated a noninvasive method for measuring the ion current [32].

The determination of the sheath capacitances in double-probe models has received considerable attention in the literature. Metze *et al.* [21] and Vallinga and de Hoog [25] calculated these capacitances assuming that the ion current at the substrate is constant. This assumption had been questioned earlier by Smy and co-workers [33,34], who pointed out that the ion continuity equation implies variations in the ion conduction current at the electrode. Smy and co-workers were unable to identify this effect experimentally, but more recent investigations have succeeded in demonstrating the effect both through numerical simulations [35] and experimental measurements [24,36]. Sobolewski, in particular, has proposed an improved model of the sheath capacitance that takes into account changes in the ion conduction current, and has shown that this model yields a better agreement with experiment than the static-sheath capacitances [24].

In the present paper we will neglect the sheath capacitance entirely. This is consistent with the low-frequency assumption, and is a good approximation whenever the sheath capacitances are smaller than the blocking capacitance. This is generally the case. With the neglect of the capacitances, the circuit equations become

$$\omega C_B \frac{d}{dt}(V_{\rm rf} - V_T) + I_- = 0, \quad (3a)$$

$$I_+ + I_- = 0. \quad (3b)$$

Introducing the ratio a of the ion saturation currents at the electrodes, $a = I_{i-}/I_{i+}$, the second circuit equation takes the form

$$1 - e^{-\varphi_f - \varphi_p} = -a(1 - e^{\varphi_T - \varphi_p - \varphi_f}),$$

where $\varphi_p = eV_p/T_e$ and $\varphi_T = eV_T/T_e$. We may solve this equation for the plasma potential in terms of the potential of the powered electrode,

$$\varphi_p(\varphi_T) = -\varphi_f + \ln\left(\frac{1 + a e^{\varphi_T}}{1 + a}\right). \quad (4)$$

Substituting this result into Eq. (2) for the current in the powered electrode yields

$$I_-(\varphi_T) = I_{i-} \frac{1 - e^{\varphi_T}}{1 + a e^{\varphi_T}}. \quad (5)$$

The above solution is illustrated in Fig. 2. We will see that a graphical analysis is particularly helpful for determining the conditions for sheath inversion.

We may now substitute the target current found in Eq. (5) into the first circuit equation (3a) to obtain a single, first-order differential equation describing the evolution of the target potential in terms of the applied bias:

$$\frac{d\varphi_T}{dt} = \frac{d\varphi_{\rm rf}}{dt} - \Phi_{B-} \frac{1 - e^{\varphi_T}}{1 + a e^{\varphi_T}}, \quad (6)$$

where

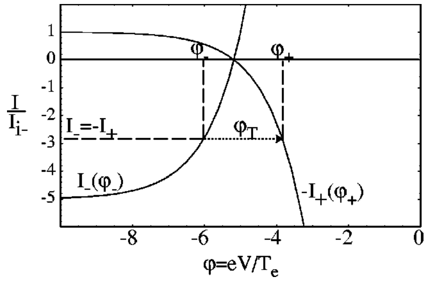

FIG. 2. Determination of the plasma potential and current in a double-sheath system with asymmetry factor $a=0.2$. The two continuous lines represent the current-voltage characteristics for the two electrodes, and the horizontal dashed line represents the target current.

$$\Phi_{B\sigma}=\frac{\sigma e I_{i\sigma}}{kT_e\omega C_B} \tag{7}$$

is the potential that would build across the blocking capacitance if it were charged with the Bohm current of the σ electrode during 1 rad or a $1/2\pi$ fraction of an oscillation cycle. Note that $\Phi_{B-}<0<\Phi_{B+}$.

Equation (6) is the central governing equation for low-frequency capacitively driven sheaths and is the principal subject of attention in the remainder of this paper. We emphasize that no accuracy has been lost in going from the original equations (1a) and (1b) of the MEO model [21] to our Eq. (6), since the original equations did not account for all the first-order effects in the small parameter $\omega_{\mathrm{rf}}/\omega_{pi}$. A comparison of the solution of Eq. (6) with the solution of the original MEO equation, shown in Fig. 3, nevertheless gives a qualitative idea of the effects of the displacement current. The parameters are

$$\begin{gathered}M=40\ \ \text{amu}\quad(\text{argon}),\quad C_B=0.5\ \ \mu\text{F},\\ n_0=10^{10}\ \ \text{cm}^{-3},\quad \omega_{\mathrm{rf}}=2\pi\times 100\ \ \text{kHz},\\ T_e=23\,200\ \ \text{K},\quad V_{\mathrm{rf}}=300\sin(\omega t)\ \ \text{V},\\ a=1,\quad A_-=100\pi\ \ \text{cm}^2.\end{gathered} \tag{8}$$

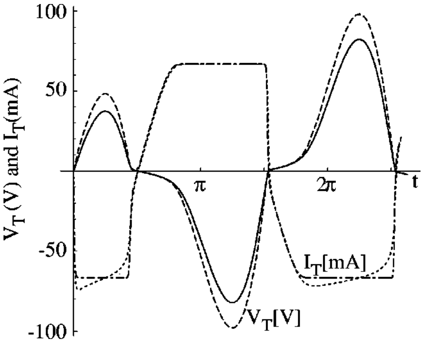

FIG. 3. Comparison of the solution of the MEO equations (1a) and (1b) for the target potential (V_T, solid line) and current (I_T, dotted line) with the solution of Eq. (6) for the target potential (dashed line) and current (dash-dotted line). The parameters are given in Eq. (8).

For these parameters $\omega_{\mathrm{rf}}/\omega_{pi}=3\%$. We have used a small blocking capacitance to accentuate the effects of the displacement current: thus, the floating sheath capacitance is an order of magnitude larger than the blocking capacitance for small sheath bias $V\sim kT_e/e$, but becomes comparatively small for sheath biases comparable to the rf bias.

We conclude this section by showing how Pointu's results [19,20] follow from Eq. (6) in the limit $C_B\to\infty$, or equivalently $\Phi_{B-}\to 0$. We expand the solution in powers of Φ_{B-} as $\varphi_T(t)=\varphi_T^{(0)}(t)+\Phi_{B-}\varphi_T^{(1)}(t)+\cdots$. To lowest order, Eq. (6) reduces to

$$\dot{\varphi}_T^{(0)}(t)=\dot{\varphi}_{\mathrm{rf}}(t),$$

where the dot indicates derivation with respect to t. Integration yields

$$\varphi_T^{(0)}(t)=\varphi_{\mathrm{rf}}(t)+\Phi_\infty. \tag{9}$$

The constant of integration Φ_∞ in Eq. (9) is a self-bias potential that is produced so as to equalize the total charge variation in each sheath during an oscillation period. The subscript ∞ indicates the fact that this integration constant applies to the fully relaxed, steady-state solution. Φ_∞ can be evaluated from the first-order equation

$$\dot{\varphi}_T^{(1)}(t)=\frac{1-e^{\varphi_T^{(0)}(t)}}{1+ae^{\varphi_T^{(0)}(t)}}.$$

In order for this equation to have a periodic solution, the right-hand side must satisfy the solubility condition

$$\oint dt\,\frac{1-e^{\varphi_{\mathrm{rf}}(t)+\Phi_\infty}}{1+ae^{\varphi_{\mathrm{rf}}(t)+\Phi_\infty}}=0. \tag{10}$$

This equation expresses conservation of charge, and is the equation used by Pointu in his analysis. It specifies implicitly the self-bias potential Φ_∞ in terms of the amplitude of the rf drive and the asymmetry a. We will consider its solution for large φ_{rf} along with the more general solutions for pulsed conditions in the following section.

III. ANALYTIC SOLUTION FOR LARGE BIAS POTENTIAL

A. Saturated and unsaturated regimes

In practical applications, the bias potential is invariably much greater than the electron temperature: $e|V_{\mathrm{rf}}|\gg kT_e$ or $|\varphi_{\mathrm{rf}}|\gg 1$. We may use this fact to obtain an analytic solution. Inspection of Eq. (6) leads to the conclusion that two regimes may occur for large φ_{rf}, corresponding to unsaturated and saturated sheaths.

In the first, unsaturated regime, the potential drop across both sheaths is negligible compared to that across the blocking capacitance and $|\dot{\varphi}_T|\ll|\dot{\varphi}_{\mathrm{rf}}|$ in Eq. (6). We may then solve for the target potential algebraically,

$$\varphi_T(t)=\ln\left(\frac{1}{a}\,\frac{\dot{\varphi}_{\rm rf}(t)-\Phi_{B-}}{\Phi_{B+}-\dot{\varphi}_{\rm rf}(t)}\right). \tag{11}$$

In this regime an electron conduction current flows through each of the sheaths. The solution given by Eq. (11) clearly requires that

$$\Phi_{B-}<\dot{\varphi}_{\rm rf}(t)<\Phi_{B+}\,. \tag{12}$$

In the case where the above condition holds for all t, Eq. (11) remains valid during the entire cycle. The sheath potentials never exceed a few volts, so that negligible ion acceleration occurs. This case is clearly of little practical interest.

For larger values of the blocking capacitance (smaller values of $|\Phi_{B\sigma}|$), we see that the solution given by Eq. (11) becomes singular when

$$\dot{\varphi}_{\rm rf}(t)=\Phi_{B\sigma}\,. \tag{13}$$

Since $\varphi_{\rm rf}$ is periodic, the above equation has two roots (modulo 2π) for each $\sigma=\pm$: we denote these roots by $t_{s,\sigma}$ and $t_{t,\sigma}$, where $t_{s,\sigma}<t_{t,\sigma}$. At the smallest (earliest) of these roots, $t_{s,\sigma}$, the system makes a transition to a second regime characterized by either $\dot{\varphi}_{\rm rf}\leqslant\Phi_{B-}$ (target sheath saturates) or $\dot{\varphi}_{\rm rf}\geqslant\Phi_{B+}$ (ground sheath saturates). The second root of Eq. (13), $t_{t,\sigma}$, represents the earliest possible time at which Eq. (12) is satisfied and the unsaturated regime may resume. As we will see below, however, the unsaturated period generally resumes much later than $t_{t,\sigma}$, if at all, due to charge accumulation by the blocking capacitor.

In the second, saturated regime the current through the plasma is equal to the ion saturation current for the saturated sheath and is constant in time. This makes it possible to integrate Eq. (6):

$$\varphi_T(t)=\varphi_{\rm rf}(t)-\Phi_{B\sigma}t+\Phi_j\,. \tag{14}$$

Here Φ_j is the integration constant for the jth saturation period, where $j=0,1,2,3,\ldots$ indexes the successive saturation periods. We adopt the convention that odd and even j label, respectively, the target and ground sheath saturations, so that $\sigma=(-1)^j$. Assuming a sinusoidal driving voltage

$$\varphi_{\rm rf}=\Phi_{\rm rf}\sin t,$$

we may write the target potential as

$$\varphi_T(t)=\Phi_{\rm rf}(\sin t-r_\sigma t)+\Phi_j\,, \tag{15}$$

where $r_\sigma=\Phi_{B\sigma}/\Phi_{\rm rf}$. The above solution, sketched in Fig. 4, contains all the information needed to assemble complete solutions of the sheath equation for arbitrary initial conditions.

We note that a solution similar to Eq. (15) was obtained previously by Kawamura *et al.* [17]. Our solution differs from theirs in two respects. First, Eq. (15) applies to the case where the blocking capacitance dominates over the sheath capacitances, $C_B\gg C_\sigma$. Kawamura *et al.*, by contrast, consider the opposite ordering. As pointed out earlier, corrections to the ion conduction currents must be taken into account when the sheath capacitance dominates. Second, in the present work we determine the constants Φ_j so as to allow for the possibility that the saturation periods succeed each other without any intervening period of time during which Eq. (12) holds and neither sheath is saturated. We discuss the determination of the Φ_j, presently.

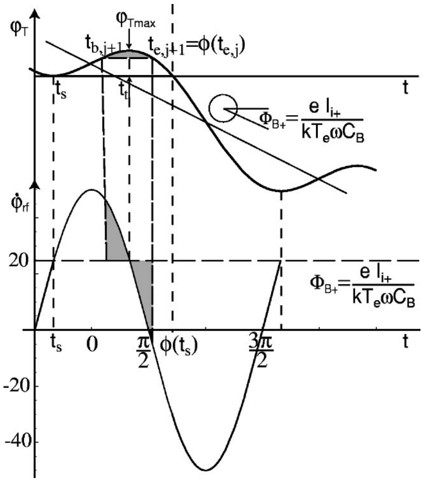

FIG. 4. Analytic solution of the low-frequency sheath equation in the saturation regime showing the relation between the earliest saturation start time, the time of maximum φ_T, and the latest return time.

B. The phase-return map

We determine the constants of integration Φ_j in Eq. (14) from the condition $\varphi_T(t_{e,j})=0$, where $t_{e,j}$ represents the time at which the jth saturation ends. Note that "zero" here means much smaller than the driving potential. The complete solution is thus specified by the sequence of end times $\{t_{e,j}\}$. We next show how to calculate these end times iteratively.

We wish to determine the end time for the $(j+1)$th saturation period knowing that the jth saturation period ended at time $t_{e,j}$. Three cases arise, depending on whether the preceding saturation period ends before, during, or after the period of time when condition (12) is violated for the electrode under consideration. We consider each case in turn.

If $t_{e,j}<t_{s,j+1}$, both sheaths remain in the unsaturated regime until the beginning of the subsequent saturation period at $t_{b,j+1}=t_{s,j+1}$. The end of this subsequent saturation period will then occur at the time $t_{e,j+1}$ specified by

$$\varphi_{\rm rf}(t_{e,j+1})-\varphi_{\rm rf}(t_{s,j+1})-\Phi_{B,j+1}(t_{e,j+1}-t_{s,j+1})=0,$$

$$t_{e,j}<t_{s,j+1}\,. \tag{16a}$$

If $t_{s,j+1}<t_{e,j}<t_{t,j+1}$, by contrast, condition (12) is violated at the end of the jth saturation and the subsequent saturation begins immediately. It will end at the time $t_{e,j+1}$ determined by

$$\varphi_{\rm rf}(t_{e,j+1})-\varphi_{\rm rf}(t_{e,j})-\Phi_{B,j+1}(t_{e,j+1}-t_{e,j})=0,$$

$$t_{s,j+1}<t_{e,j}<t_{t,j+1}\,. \tag{16b}$$

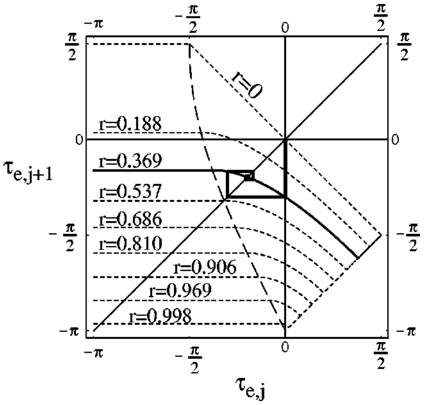

FIG. 5. Phase-return maps for a series of values of r (dotted lines). The case $r=0.369$ is shown as a continuous line. The segmented spiral represents the sequence of end times for a symmetric discharge with this value of r. The dashed line represents the locus of times such that the preceding (jth) saturation period ends at the natural onset time τ_s defined by Eq. (13), i.e., $\tau_{e,j}=\tau_s$.

Finally, if $t_{t,j+1}<t_{e,j}$, the $(j+1)$th saturation period is avoided entirely. Equivalently, it may be considered to end immediately upon the end of the jth saturation period,

$$t_{e,j+1}=t_{e,j}, \quad t_{t,j+1}<t_{e,j}. \tag{16c}$$

Equations (15) and (16a)–(16c) constitute the main result of this section. Together, Eqs. (16a)–(16c) uniquely specify the end $t_{e,j+1}$ of the $(j+1)$th saturation period in terms of the end $t_{e,j}$ of the jth saturation period for different values of the blocking capacitance and asymmetry. This allows the complete solution to be constructed for arbitrary initial conditions by concatenating successive instances of the saturated solution given in Eq. (15) .

It is convenient to divide the oscillations into half cycles and to record the return times modulo π, so as to measure their time of occurrence relative to a reference half cycle. We thus define the relative end time τ_e by $\tau_{e,j+1}=t_{e,j+1}-j\pi$. In terms of the relative times and for a sinusoidal drive, Eq. (16a)–(16c) take the form

$$\sin(\tau_{e,j+1})+\sin(\tau_{s,\sigma})+|r_\sigma|(\tau_{e,j+1}+\pi-\tau_{s,j})=0,$$

$$\tau_{e,j}<\tau_{s,\sigma}, \tag{17a}$$

$$\sin(\tau_{e,j+1})+\sin(\tau_{e,j})+|r_\sigma|(\tau_{e,j+1}+\pi-\tau_{e,j})=0,$$

$$\tau_{s,\sigma}<\tau_{e,j}<\tau_{t,\sigma}, \tag{17b}$$

$$\tau_{e,j+1}+\pi-\tau_{e,j}=0, \quad \tau_{t,\sigma}<\tau_{e,j}, \tag{17c}$$

where $\sigma=(-1)^{j+1}$. Equations (17a) and (17b) may be visualized as a map $\tau_{e,j+1}=\phi(\tau_{e,j})$ from the reference period onto itself, as shown in Fig. 5. This map is a special case of Poincaré's map of first return, and we will refer to it as the phase-return map. The dashed line in Fig. 5 represents the locus of points such that $\tau_{e,j}=\tau_{s,\sigma}$ for $\sigma=(-1)^{j+1}$, or such that the jth saturation ends precisely at the natural onset point for the $(j+1)$th saturation given by Eq. (13). In the region to the left of this dashed line, successive saturation periods are separated by an unsaturated regime. In this region the onset of the saturation periods is given by Eq. (13) and is independent of the end of the previous saturation period, hence the curves for $\tau_{e,j+1}$ are horizontal.

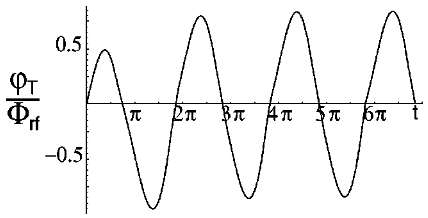

FIG. 6. Analytic solution φ_T for $r=0.369$, corresponding to the solid line in Fig. 5.

The phase-return map gives a straightforward way of charting graphically the evolution of the sheath biases. The procedure is illustrated in Fig. 5 for a symmetric discharge, where $\Phi_{B-}=\Phi_{B+}=\Phi_B$. Assuming that $\Phi_{\rm rf}>\Phi_B$, the ground sheath saturates immediately at $\tau=0$ and we may take $\tau_{e,-1}=0$. The first saturation period will then end at $\tau_{e,0}$, given by the intersection of the vertical at $\tau=0$ with the curve corresponding to the appropriate value of Φ_B for the discharge. We refer to this as the first intersection point. The end time for the first saturation period may then be carried back to the abscissa by finding the intersection of the horizontal line going through the first intersection point with the diagonal line going through the origin. The return time for the second saturation period is now given by the intersection of the vertical line going through the second starting time with the appropriate phase-return curve. This process may be repeated indefinitely and is easily automated. For an asymmetric discharge, one needs only to alternate between the two curves corresponding to the ground and target sheaths. The analytic solution constructed by piecing together the successive saturation solutions (15) is shown in Fig. 6. For $\Phi_T>50$ it is almost indistinguishable from the numerical solution of Eq. (6).

In the following sections, we will show how the phase-return map can be used to evaluate the steady-state parameters, and we will consider the relaxation behavior of pulsed discharges.

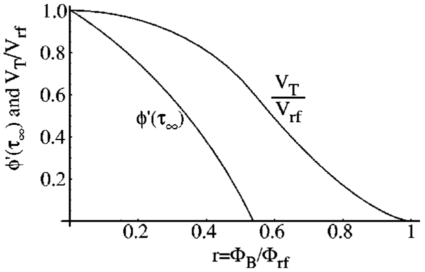

FIG. 7. Amplitude of the target electrode potential $V_T/V_{\rm rf}$ and convergence multiplier $\phi'(\tau_\infty)$ for a symmetric discharge as a function of the inverse of the blocking capacitance, parametrized by the ratio $r=\Phi_B/\Phi_{\rm rf}$

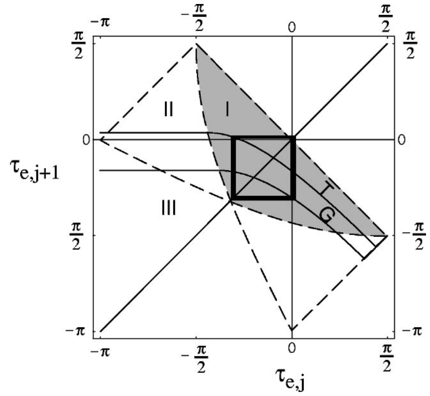

FIG. 8. Phase-return maps for an asymmetric discharge with a large blocking capacitance (regime I). Note that the sequence of end times is found by alternating between the phase-return curves corresponding to the ground and target sheaths. $r_-=0.188$ and $r_+=0.369$, corresponding to $a=0.509$.

IV. STEADY-STATE SOLUTIONS AND TRANSIENT RELAXATION

A. Symmetric electrodes

For symmetric discharges, Fig. 5 shows that steady-state solutions correspond to the limit points of the phase-return map. These limit points are found as the intersection of the phase-return curves with the diagonal representing $\tau_{e,j+1}=\tau_{e,j}$. Two cases must be distinguished depending on whether the limit point is in the regime where successive saturation periods are separated by an unsaturated regime (left of the dashed line) or where saturation regimes succeed each other without a pause. This is determined by the value of the blocking capacitance. The marginal value of the capacitance separating these two cases is such that the end time follows the singular time τ_s after exactly half a period, $\tau_{e,j+1}=\tau_{s,j}$. Substituting this in Eq. (17a) yields

$$\sin\tau_s=r\pi/2.$$

For a symmetric discharge with a sinusoidal drive, Eq. (13) defining τ_s takes the form

$$\cos\tau_s=r.$$

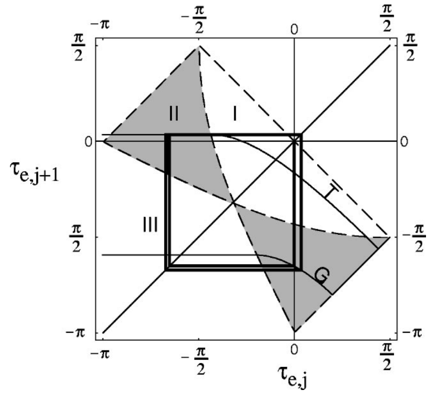

FIG. 9. Phase-return map for an asymmetric discharge with a moderate value of the blocking capacitance (regime II). $r_-=0.188$ and $r_+=0.810$, corresponding to $a=0.232$.

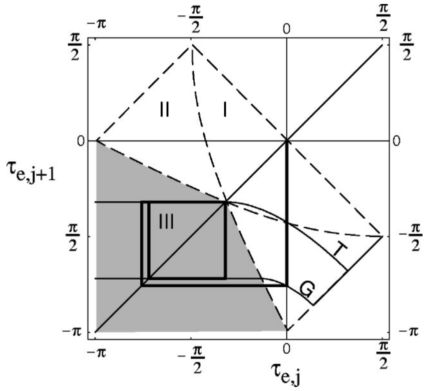

FIG. 10. Phase-return map for an asymmetric discharge with a small value of the blocking capacitance (regime III). $r_-=0.537$ and $r_+=0.906$, corresponding to $a=0.593$.

We may eliminate τ_s by summing the squares of the above two equations. This yields the marginal value of r,

$$r_{\rm marg}=(1+\pi^2/4)^{-1/2}\simeq 0.73. \tag{18}$$

Reverting to dimensional variables, we conclude that for

$$1<\frac{e\omega_{\rm rf}C_B}{T_eI_i}<(1+\pi^2/4)^{1/2}, \tag{19}$$

the saturation periods will be separated by unsaturated periods, as assumed by Kawamura *et al.* For smaller values of C_B, the sheaths will never saturate at all, while for large values of C_B the saturation periods will succeed each other without a pause.

The maximum amplitude of the target potential is reached at the time τ_t corresponding to the second root of Eq. (13). The value of the amplitude at this time depends on the integration constant Φ_∞. For $r_{\rm marg}<r<1$,

$$\varphi_{\max}=\Phi_{\rm rf}[\sin\tau_t-\sin\tau_s-r(\tau_t-\tau_s)].$$

Using Eq. (13) to evaluate the τ's yields

$$\varphi_{\max}=\Phi_{\rm rf}[2(1-r^2)^{1/2}-2r\cos^{-1}r], \quad r_{\rm marg}<r<1.$$

A similar calculation for $r<r_{\rm marg}$ yields

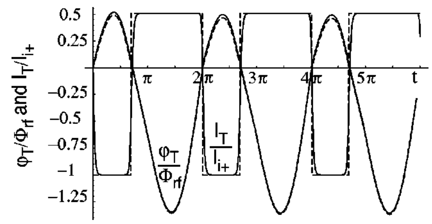

FIG. 11. Time evolution of the normalized target potential $\varphi_T(t)$ and current $I_T(t)$ for the parameters of Fig. 8. The continuous lines represent the numerical solution and the dashed lines represent the analytic solution. The driving potential $V_{\rm rf}=50$ V, and the plasma parameters are as in Eq. (8).

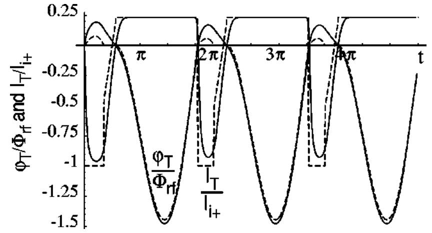

FIG. 12. Time evolution of the normalized target potential $\varphi_T(t)$ and current $I_T(t)$ for the parameters of Fig. 9. The continuous lines represent the numerical solution and the dashed lines represent the analytic solution. The driving potential $V_{\rm rf}=50$ V and the plasma parameters are as in Eq. (8).

$$\frac{\varphi_{max}}{\Phi_{\rm rf}}=-\left[r\left(\pi-\cos^{-1}r-\sin^{-1}\frac{r\pi}{2}\right)\right.$$
$$\left.+\frac{r\pi}{2}-(1-r^2)^{1/2}\right],\quad 0<r<r_{\rm marg}.$$

The above results are plotted as a function of r in Fig. 7.

B. Asymmetric electrodes

In the case of asymmetric discharges, steady-state solutions correspond to limit cycles of the phase-return map. Geometrically, they appear as squares with two vertices lying on the diagonal $\tau_{e,j+1}=\tau_{e,j}$ (Fig. 8–109). Three regimes can be distinguished depending on the occurrence of unsaturated periods following the target- and ground-saturation periods. These regimes can be identified graphically by the position of the off-diagonal vertices of the limit cycle with respect to the locus of singular times represented by the dashed line in the phase-return maps. The analytic solutions for all three regimes are compared to the numerical solutions of Eq. (6) in Figs. 11–13. We used an unusually low source potential in these figures, $V_{\rm rf}=50$ V, so as to accentuate the difference between the analytic and numerical solutions. We next describe the three regimes in turn.

In the first regime, when the vertices of the limit cycle lie in the region labeled I and shaded in Fig. 8, one of the sheaths is always saturated. The saturation end times are then determined by applying Eq. (17b) at each sheath:

$$\sin(\tau_{e,+})+\sin(\tau_{e,-})+r_+(\pi+\tau_{e,+}-\tau_{e,-})=0,\quad (20a)$$

$$\sin(\tau_{e,+})+\sin(\tau_{e,-})+r_-(\pi+\tau_{e,-}-\tau_{e,+})=0.\quad (20b)$$

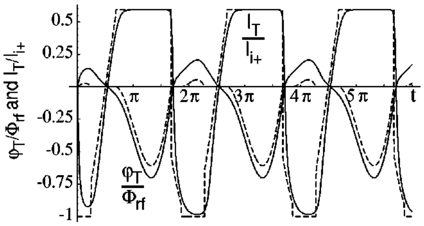

FIG. 13. Time-evolution of the normalized target potential $\varphi_T(t)$ and current $I_T(t)$ for the parameters of Fig. 10. The continuous lines represent the numerical solution and the dashed lines represent the analytic solution. The driving potential $V_{\rm rf}=50$ V and the plasma parameters are as in Eq. (8).

Equations (20a) and (20b) may be solved for the end times. We find that the duration of the ground sheath saturation period is

$$\tau_{e-}-\tau_{e+}=\pi\frac{1-a}{1+a}.\quad (21)$$

Surprisingly, the durations of the saturation periods are independent of the value of the blocking capacitance: this result is thus identical to that found earlier by Pointu [19,20] and Song, Field, and Klemperer [26] for the limit $C_B\rightarrow\infty$.

The center of the saturation intervals measures the phase shift between the applied rf signal and the target potential: it is given by the solution of

$$\sin\left(\frac{\tau_{e+}+\tau_{e-}}{2}\right)=-\frac{\pi a r_+}{1+a}\left[\cos\left(\pi\frac{1-a}{1+a}\right)\right]^{-1}.\quad (22)$$

We see that the phase shift, unlike the duration of the saturation period, does depend on the value of the blocking capacitance.

In the second regime, labeled II in Fig. 9, the target-saturation period is preceded by an unsaturated period. In this regime, Eq. (20b) must be replaced by

$$\sin(\tau_{e,-})+\sin(\tau_{s,-})+r_-(\pi+\tau_{e,-}-\tau_{s,-})=0.\quad (23)$$

The evolutions of φ_T and I_T in this regime are shown in Fig. 12.

Lastly, in regime III there are unsaturated periods preceding both the target- and ground-saturation periods. In this case the steady-state end times are determined by Eq. (23) and

$$\sin(\tau_{e,+})+\sin(\tau_{s,+})+r_+(\pi+\tau_{e,+}-\tau_{s,+})=0.\quad (24)$$

The evolutions of φ_T and I_T in regime III are shown in Fig. 13.

C. Relaxation rate

We next consider the convergence properties for nonstationary discharges. In the case of symmetric discharges, the phase-return map specifies that the return time for the $(j+1)$th time is given in terms of that for the jth time by

$$\tau_{j+1}=\phi(\tau_j),$$

where ϕ is the phase-return function. The stationary point is thus the solution of

$$\tau_\infty=\phi(\tau_\infty).$$

Linearizing about the stationary point, we see that the distance to this point is multiplied at each step by $\phi'(\tau_\infty)$:

$$\delta\tau_{j+1}=\phi'(\tau_\infty)\delta\tau_j,$$

where $\delta\tau_j=\tau_j-\tau_\infty$. It follows that for small values of the capacitance, when the saturation period does not extend over the entire half-period $(r_{\rm marg}<r<1),\phi'=0$ and the steady state is reached in a single half-period. In the opposite limit

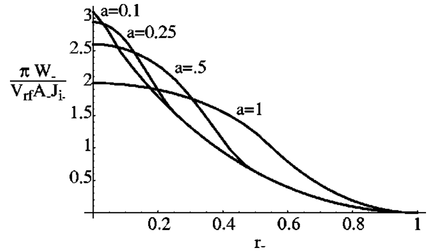

FIG. 14. Variation of the time-averaged power with the parameter r_- proportional to the inverse of the blocking capacitance for four values of the asymmetry coefficient a.

of large capacitance, $\phi' \to -1$ and convergence becomes slow. For intermediate values of $r, 0 < r < r_{\mathrm{marg}}$, the convergence factor is

$$\phi'(\tau_\infty) = r - \sqrt{1 - r^2\pi^2/4}. \tag{25}$$

The convergence factor $|\phi'(\tau_\infty)|$ is shown in Fig. 7.

In asymmetric discharges, the convergence factor is obtained simply by multiplying the convergence factors for each of the two sheaths.

$$\delta\tau_{j+1} = \phi'(\tau_+)\phi'(\tau_-)\delta\tau_j,$$

where $\tau_\pm$ are the asymptotic end times for the ground- and target-saturation periods. In general, as can be seen from the phase-return diagram of Fig. 7, the ground sheath falls in a regime where $\phi'(\tau_+) \simeq -1$. The convergence factor is thus approximately given by $\phi'(\tau_-)$.

D. Power dissipation

The power dissipated in the sheaths is easily calculated from the analytic expressions for the target potential (14) and current (5). Integrating the power dissipated from the beginning time t_b to the end time t_e of a saturation period, we find

$$W_{\mathrm{sat},\pm} = \mp V_{\mathrm{rf}} I_{\mathrm{sat}} (\cos t_{e,\pm} - \cos t_{b,\pm}), \tag{26}$$

where $W_{\mathrm{sat},+}$ and $W_{\mathrm{sat},-}$ are, respectively, the work done during the ground- and target-saturation periods. During the unsaturated periods, by contrast, the circuit current is found by neglecting the target potential in Eq. (6). The integrated power is then

$$W_{\mathrm{uns},\pm} = \omega C_B \frac{V_{\mathrm{rf}}^2}{2} (\sin^2 t_{b,\pm} - \sin^2 t_{e,\mp}), \tag{27}$$

where $t_{e\pm} = t_{b\mp}$ in the absence of the corresponding unsaturated period. Summing the above two expressions for the saturated and (eventual) unsaturated periods with the appropriate start and end times and dividing by the period yields the average power

$$W = \frac{V_{\mathrm{rf}} I_{i-}}{2\pi} [(\cos\tau_{e+} + \cos\tau_{b+})/a + \cos\tau_{e-} + \cos\tau_{b-} + (\sin^2\tau_{b+} - \sin^2\tau_{e+} + \sin^2\tau_{b-} - \sin^2\tau_{e-})/r_-]. \tag{28}$$

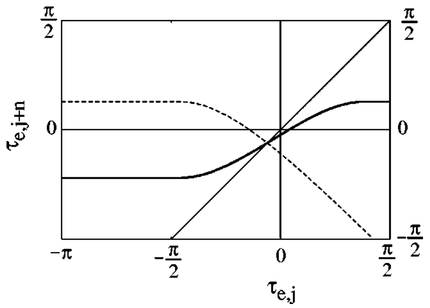

FIG. 15. Map of first (dotted line) and second (continuous line) returns for $r = 0.12$. The fact that both maps have the same steady-state solution, represented by their point of intersection with the diagonal, shows that there is no period 2 orbit for capacitively coupled sheaths.

The variation of the power with the blocking capacitance for different values of the asymmetry factor a is shown in Fig. 14. In general, the beginning and end times of the saturation periods must be obtained numerically. For symmetric discharges without saturation periods, however, the power may be given in the closed analytic form

$$W = \frac{2V_{\mathrm{rf}} I_{i-}}{\pi} \sqrt{1 - \frac{\pi^2 r^2}{4}}. \tag{29}$$

In the limit of large blocking capacitance, the power may also be written in the closed analytic form

$$W = V_{\mathrm{rf}} I_{i-} \frac{1+a}{a\pi} \sin\left(\frac{a\pi}{1+a}\right). \tag{30}$$

The above results are in excellent agreement with those obtained by direct integration of the numerical solutions of Eq. (6).

E. Period doubling

Period doubling has been demonstrated in capacitively coupled sheaths driven by a resonantly tuned circuit by Miller *et al.* [37]. For the simple capacitive coupling considered here, however, we find no occurrence of period doubling. This is easily seen by examining the map of second return obtained by applying the phase-return map to itself (Fig. 15). The second-return map has only one steady-state solution, corresponding to its single point of intersection with the diagonal. This steady state is identical to that for the single-period map. This shows that period doubling does not occur in the absence of resonant tuning, in agreement with the results of Miller *et al.* [37].

F. Optimal blocking capacitance

For electron-ion sheaths, the optimal blocking capacitance is determined by maximizing the coupling of the source to the target sheath while avoiding ground sheath saturation. At first sight this is accomplished by taking the largest capacitance such that the saturation of the ground sheath is impossible (even transiently),

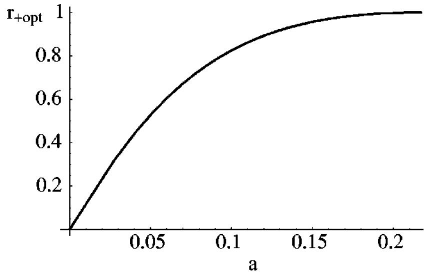

FIG. 16. Optimum value of r_+ as a function of the aspect ratio a.

$$C_B \leqslant \frac{I_{i+}}{\omega V_{\mathrm{rf}}}. \tag{31}$$

If transient ground sheath saturation is acceptable, however, the self-bias potential may allow a larger capacitance to be used while avoiding ground sheath saturation in the steady state. This larger capacitance improves the rf coupling to the target sheath. The reason ground saturation is avoided in steady state is that the saturation period for the target sheath lasts so long that it overshoots the range of times when ground sheath saturation could occur. The optimum value of r_+, when transient ground saturation is tolerated, follows by equating the steady-state end time for the target-saturation period t_{e-} to the upper limit t_t of the range of time during which $\dot{\varphi}_{\mathrm{rf}}(t) > \Phi_{B+}$. In the absence of a ground-saturation period, the end of the target sheath saturation is $\tau_{e-} = \phi(\tau_{s-})$. The optimal capacitance is thus determined by

$$\tau_{t+} = \phi(\tau_{s-}),$$

where τ_{t+} and τ_{s-} are determined by Eq. (13). The corresponding optimal value of r_+ is plotted as a function of the aspect ratio in Fig. 16. Note that the steady-state optimum for r_+ differs from unity only for sufficiently small values of a. Specifically, $r_{+\mathrm{opt}}$ reaches unity for $\tan \tau_{s-} + \pi = \tau_{s-}$, or $t_{s-} = -1.352$. Evaluating the corresponding a yields $a_{\mathrm{marg}} = r_- = \cos t_{s-} = 0.217$. For larger values of $a, a > a_{\mathrm{marg}}$, the optimum capacitance is given by Eq. (31).

V. NEGATIVE-ION EXTRACTION

A persistent problem when using rf-driven sheaths for etching is that comparatively few electrons reach the bottom of large aspect-ratio trenches due to the isotropy of the electron flux as opposed to the anisotropy of the ion flux [38–41]. This results in differential charging of the surface of the substrate with respect to the bottom of the trenches. The consequent ohmic heating and the perturbation of the ion trajectories caused by the field are a significant source of fabrication damage.

An approach to solving the charging problem is to force the inversion of the sheath potential so as to attract negative ions into the trenches. Numerical simulations [11] and recent experiments [9,10,12,13] have demonstrated that negative-ion extraction is achievable in the afterglow of pulsed discharges. During the power-off phase, negative ions are formed by dissociative attachment, thereby producing strongly electronegative discharges that approach, in some cases, pure ion-ion plasmas [2,6,7,42,43]. Equal doses of negative and positive ions can then be extracted by applying an rf bias to the substrate during the afterglow phase. Of course, the rf frequency must be smaller than the ion plasma and transit frequencies to allow the ions to respond to the rf field.

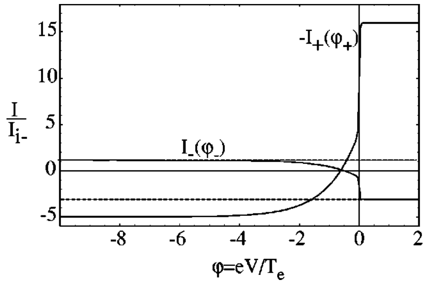

FIG. 17. Current-voltage characteristics in a negative-ion dominated plasma with electronegativity $\alpha = 100$ and mass ratio $m_n/m_p = 2$ (appropriate for Cl^+-Cl_2^-).

In order to extend the analysis presented in Secs. II and III to electronegative plasmas, one needs only to know the current-voltage characteristics for such plasmas. In principle, determination of the current-voltage characteristics requires the use of kinetic theory, since the negative and positive ions have comparable temperatures. Fortunately, we have seen in the preceding section that for strong bias, the dynamics of the sheath is dominated by periods in which one of the sheaths is saturated. The ion currents, in particular, are essentially always either saturated or cut off due to the high values of the bias compared to the ion temperature. This makes it possible to draw some useful conclusions from a simple fluid model.

We thus extend the model of Sec. II to negative ions by using the following fluid-theory-based expression for the current characteristics:

$$I_\sigma = \begin{cases} A_\sigma\left[n_p e u_{Bp} - \dfrac{1}{4} n_e e \bar{v}_e \exp(\varphi_\sigma)\right], & \varphi \leqslant -1/\gamma \\ -A_\sigma\left[\dfrac{1}{4} n_e e \bar{v}_e + n_n e u_{Bn}\right], & 1/\gamma \leqslant \varphi, \end{cases} \tag{32}$$

where u_{Bp} and u_{Bn} are the Bohm saturation currents for positive- and negative-ion extraction, respectively, $\alpha = n_p/n_e$ is the electronegativity, $\gamma = T_e/T_i$ is the temperature ratio (we assume here $T_p = T_n = T_i$), and $\bar{v}_e = \sqrt{8T_e/\pi m_s}$ is the electron thermal velocity. The Bohm fluxes in electronegative plasmas [28,31] are

$$u_{Bs}^2 = \frac{\Gamma k T_s}{m_s} + \frac{kT_e}{m_s} \frac{1+\alpha}{1+\alpha\gamma} \simeq (1+\Gamma) \frac{kT_s}{m_s} \tag{33}$$

where Γ is the adiabatic expansion constant and where the approximate form on the right holds for $\alpha \gg 1$. The above current-voltage characteristics are shown in Fig. 17.

We next obtain the condition for sheath inversion. From Fig. 17, we see that sheath inversion occurs when the negative saturation current at the target electrode is of a lesser magnitude than the ion saturation current at the ground electrode,

$$A_-(n_{n-}u_{Bn-}+n_{e-}\overline{v}_e/4)<A_+n_{p+}u_{Bp+}, \qquad (34)$$

where we have included sheath indices to allow for the possibility that the density and temperatures are different at the two electrodes. For strong electronegativity ($n_p \simeq n_n$), the above criterion simplifies to

$$\alpha > \frac{a\sqrt{\dfrac{m_pT_e}{2\pi m_eT_i}}}{1-a\sqrt{\dfrac{m_p}{m_n}}}. \qquad (35)$$

We see that inversion is helped by low electron temperature and by high reactor asymmetry. Note that for $m_p=m_n, a<1$ is necessary for sheath inversion. Experimental observations have shown that the electron temperature falls rapidly in the afterglow phase, facilitating sheath inversion. In inductively coupled chlorine discharges, for example, Ahn *et al.* [42] have shown that at the beginning of the power-off phase, the electron temperature drops at time of the order of 10 μs, while the electron density drops somewhat more slowly, at time of the order of 25 μs. The density of Cl^- ions rises concomitantly with the fall of the electron density due to dissociative attachment.

The results of Sec. III remain applicable when the sheath inversion criterion (35) is satisfied, provided that the proper values of the saturation currents are used. Specifically, the ground sheath ion saturation current must be replaced by the target sheath negative saturation current, and the ''ground-saturation'' period must now be reinterpreted as a target sheath inversion period. We may then use these results to discuss the role of the blocking capacitance.

When the sheath inversion criterion is only marginally satisfied, large values of the capacitance favor negative-ion extraction by drawing more negative current out of the target electrode [11]. When the sheath inversion criterion is well satisfied, by contrast, the choice of the blocking capacitance is governed by the need to maintain good response time while ensuring that both positive and negative saturations are achieved. The response time is of concern, since the afterglow period typically lasts for only a few rf periods, and failure to relax to the steady-state condition would result in differential charging, precisely the condition that negative-ion extraction seeks to remedy. Examination of the results of Sec. III shows that relaxation is achieved in a single cycle if the saturation periods are separated by an (however brief) unsaturated period. We conclude that the optimum capacitance in this case is such as to place the system at the boundary between regimes I and II (Fig. 9).

VI. SUMMARY

We have investigated the dynamics of a two-sheath system driven capacitively by an rf source. We based our analysis on the observation that the sheath displacement currents are small in the limit of low frequency and can be neglected in the presence of a large blocking capacitance, $C_B \gg C_s$. The system can then be described by a single first-order differential equation, Eq. (6).

We have solved analytically Eq. (6) governing sheath dynamics in the limit $eV_{\mathrm{rf}}/kT_e \gg 1$. Our solution may be viewed as a generalization of the analytic solutions of Pointu [19,20] ($C_B \rightarrow \infty$) to finite values of the blocking capacitances satisfying $C_B \gg C_s$ and to nonstationary conditions. We have shown that the properties of the dynamics are most easily understood in terms of the phase-return map describing the times at which successive saturation periods end. This map is a special case of Poincaré's map of first return, and provides a convenient way of predicting the properties of the solutions and the role of factors such as the blocking capacitor and asymmetry.

The blocking capacitance has two effects on the sheath-circuit dynamics. First, it determines the duration of the sheath saturation periods. Second, it determines the rate of relaxation to steady state in pulsed discharges. The magnitude of these effects is most conveniently measured by comparing the blocking capacitance to a characteristic capacitance for the system defined as the capacitance that would be charged up to the driving voltage V_{rf} by the negative saturation current to the target electrode, I_{sat}, in a time equal to $1/2\pi$ of the source period,

$$C_{\mathrm{char}}=\frac{I_{\mathrm{sat}}}{\omega V_{\mathrm{rf}}}. \qquad (36)$$

For electron-ion sheaths I_{sat} is equal and opposite to the positive-ion saturation current for the *ground* sheath. For ion-ion sheaths, by contrast, it is given by the negative-ion saturation current for the *target* sheath.

In asymmetric discharges, the most salient effect of relaxation is the buildup of a self-bias potential ensuring conservation of current across the discharge. In symmetric discharges, by contrast, there is no self-bias, so that the relaxation is observed more subtly as a phase adjustment.

For electron-ion sheaths, the optimum capacitance is determined by maximizing the rf coupling to the sheath while avoiding ground sheath saturation. Ground sheath saturation is undesirable, as the attendant wall bombardment by energetic ions results in impurity release and wall damage. For an asymmetry factor $a>0.217$, the optimum capacitance is equal to the characteristic capacitance defined in Eq. (36) above. For $a<0.217$, by contrast, the ratio of the characteristic capacitance to the optimal capacitance becomes less than unity, as shown in Fig. 16.

For negative-ion dominated sheaths, ground saturation must be avoided by adopting a reactor asymmetry such that $a<\sqrt{m_n/m_p}$ [cf. Eq. (35)] [13]. The optimum blocking capacitance is then determined by balancing the requirements of good sheath coupling and rapid relaxation so as to avoid substrate charging.

ACKNOWLEDGMENTS

The authors benefited from helpful discussions with S. Hamaguchi and S. Kanaksabapathy. This work was supported by U.S. DOE, Contract No. DE-FG03-96ER-54346.

[1] N. Hershkowitz, IEEE Trans. Plasma Sci. **26**, 1610 (1998).
[2] J.T. Verdeyen, J. Beberman, and L. Overzet, J. Vac. Sci. Technol. A **8**, 1851 (1990).
[3] H. Sugai, K. Nakamura, Y. Hikosaka, and M. Nakamura, J. Vac. Sci. Technol. A **13**, 887 (1995).
[4] S. Ashida and M.A. Lieberman, J. Vac. Sci. Technol. A **13**, 2498 (1995).
[5] S. Ashida, M.R. Shim, and M.A. Lieberman, J. Vac. Sci. Technol. A **14**, 391 (1996).
[6] J.P. Booth and N. Sadeghi, J. Appl. Phys. **70**, 611 (1991).
[7] A. Kono, M. Haverlag, G.M.W. Kroesen, and F.J. de Hoog, J. Appl. Phys. **70**, 2939 (1991).
[8] T. Trottenberg, A. Melzer, and A. Piel, Plasma Sources Sci. Technol. **4**, 450 (1995).
[9] T. Shibayama, H. Shindo, and Y. Horiike, Plasma Sources Sci. Technol. **5**, 254 (1996).
[10] S. Samukawa and T. Mieno, Plasma Sources Sci. Technol. **5**, 132 (1996).
[11] S.K. Kanakasabapathy and L.J. Overzet, Plasma Sources Sci. Technol. **7**, 289 (1998).
[12] S.K. Kanakasabapathy, M.H. Khater, and L.J. Overzet, Appl. Phys. Lett. **79**, 1769 (2001).
[13] S.K. Kanakasabapathy, L.J. Overzet, V. Midha, and D. Economou, Appl. Phys. Lett. **78**, 22 (2001).
[14] P.A. Miller, H. Anderson, and M.P. Splichal, J. Appl. Phys. **71**, 1171 (1992).
[15] P.J. Hargis, Jr. *et al.*, Rev. Sci. Instrum. **65**, 140 (1994).
[16] S. Rauf and M.J. Kushner, J. Appl. Phys. **83**, 5087 (1998).
[17] E. Kawamura, V. Vahedi, M.A. Lieberman, and C.K. Birdsall, Plasma Sources Sci. Technol. **8**, R45 (1999).
[18] M.A. Lieberman, IEEE Trans. Plasma Sci. **16**, 638 (1988).
[19] A.M. Pointu, Appl. Phys. Lett. **48**, 762 (1986).
[20] A.M. Pointu, J. Appl. Phys. **60**, 4113 (1986).
[21] A. Metze, D.W. Ernie, and H.J. Oskam, J. Appl. Phys. **60**, 3081 (1986).
[22] P.A. Miller and M.E. Riley, J. Appl. Phys. **82**, 3689 (1997).
[23] W.M. Manheimer, IEEE Trans. Plasma Sci. **28**, 359 (2000).
[24] M.A. Sobolewski, Phys. Rev. E **62**, 8540 (2000).
[25] P.M. Vallinga and F.J. de Hoog, J. Phys. D **22**, 925 (1989).
[26] Y.P. Song, D. Field, and D.F. Klemperer, J. Phys. D **23**, 673 (1990).
[27] M. Klick, Phys. Rev. E **47**, 591 (1993).
[28] R.N. Franklin and J. Snell, J. Phys. D **25**, 453 (1992).
[29] R.N. Franklin, Plasma Sources Sci. Technol. **9**, 191 (2000).
[30] R.N. Franklin, Plasma Sources Sci. Technol. **10**, 162 (2001).
[31] K.U. Riemann, IEEE Trans. Plasma Sci. **4**, 709 (1995).
[32] M.A. Sobolewski, Appl. Phys. Lett. **72**, 1146 (1998).
[33] P.R. Smy and J.R. Greig, J. Phys. D **1**, 351 (1968).
[34] P.R. Smy, J.A. Nation, and D. Simpson, J. Phys. D **2**, 1095 (1968).
[35] W. Goedheer and P. Meijer, IEEE Trans. Plasma Sci. **19**, 245 (1998).
[36] M.A. Sobolewski, Phys. Rev. E **59**, 1059 (1999).
[37] P.A. Miller, L.A. Romero, and P.D. Pochan, Phys. Rev. Lett. **71**, 863 (1993).
[38] J.C. Arnold and H.H. Sawin, J. Appl. Phys. **70**, 5314 (1991).
[39] G.S. Hwang and K.P. Giapis, J. Vac. Sci. Technol. B **15**, 70 (1996).
[40] T. Kinoshita, M. Hane, and J.P. McVittie, J. Vac. Sci. Technol. B **14**, 560 (1996).
[41] J. Matsui, N. Nakano, Z.L. Petrovic, and T. Makabe, Appl. Phys. Lett. **78**, 883 (2001).
[42] T.H. Ahn, K. Nakamura, and H. Sugai, Plasma Sources Sci. Technol. **5**, 139 (1996).
[43] M.V. Malyshev, V.M. Donnelly, J.I. Colonell, and S. Samukawa, J. Appl. Phys. **86**, 4813 (1999).